ADVANCED OPTICAL MATERIALS
www.advopticalmat.de

# Boosting the Performance of Epitaxial Perovskite Microstructures by Surface Passivation

*Shuyu Zhou, Viktor Rehm, Roman Grizfeld, Zihao Liu, Yufei Han, Tomáš Hrbek, Iva Matolínová, Jędrzej Korczak, Andrzej Szczerbakow, Tomasz Story, Mordechai Kot, Maria A. Loi, Zijian Peng, Masato Sotome, Takashi Kondo, Karen Forberich, Larry Lüer, Christoph. J. Brabec, Julia Mergheim, and Wolfgang Heiss**

**Epitaxial growth enables the fabrication of films and heterostructures with exceptional properties, particularly when performed on single-crystalline substrates with a suitable lattice type and lattice parameters. While epitaxial growth is extensively utilized for conventional semiconductors, epitaxial micro- and nanostructures of lead-halide perovskites have also been successfully obtained through vapor-phase and liquid-phase deposition techniques. Surface passivation, widely employed in polycrystalline perovskite films and single crystals to suppress surface recombination of charge carriers, is often overlooked for epitaxial structures due to the presumption that their inherently smooth surfaces are free of defects. In this study, surface passivation agents commonly used in colloidal nanocrystal chemistry are investigated, such as trioctylphosphine oxide (TOPO), or protective matrices like poly (methyl methacrylate) (PMMA), to improve the performance of epitaxially grown Formamidinium lead bromide ($FAPbBr_3$) and Cesium lead bromide ($CsPbBr_3$) micro- and nanostructures. These findings reveal that surface passivation significantly boosts luminescence intensity and decay times, reduces lasing thresholds to record-low levels for microcrystalline perovskite lasers, and enhances the specific detectivity of photoconductors. These advancements are consistent across structures grown by both vapor deposition and solution processing. This study highlights the critical role of surface passivation for achieving the full potential of epitaxially grown perovskite structures, thereby paving the way for advanced optoelectronic applications.**

## 1. Introduction

Epitaxial growth of semiconductors is a cornerstone technique for realizing their maximum performance potential. In advanced silicon technology, high-quality polished silicon wafers serve as substrates for epitaxial layers with properties finely tailored to differ from the underlying material. This approach is indispensable for the fabrication of highly integrated circuits[1,2] and high-power electronic devices[3] The success of semiconductor laser diodes depends on the epitaxial growth of III-V semiconductor heterostructures,[4] as well as the development of white light-emitting diodes that are replacing incandescent lamps.[5] These epitaxially grown structures, produced at an industrial scale, are foundational to modern technology and pervasive in daily life. The strength of epitaxial growth lies in its unparalleled precision, enabling the sequential deposition of atomic layers with varying compositions to form coherent interfaces between materials with differing bandgap energies. This precise engineering of band gaps within epitaxial heterostructures

S. Zhou, V. Rehm, R. Grizfeld, Y. Han, Z. Peng, L. Lüer, C. J. Brabec, W. Heiss
Institute of Materials for Electronics and Energy Technology (i-MEET)
Department of Materials Science and Engineering
Friedrich-Alexander-Universität Erlangen-Nürnberg
Martensstrasse 7, 91058 Erlangen, Germany
E-mail: wolfgang.heiss@fau.de

The ORCID identification number(s) for the author(s) of this article can be found under https://doi.org/10.1002/adom.202503210



**DOI: 10.1002/adom.202503210**

S. Zhou, V. Rehm, R. Grizfeld, Y. Han, C. J. Brabec, W. Heiss
Institute-Materials for Electronics and Energy Technology (i-MEET)
Department of Materials Science and Engineering
Friedrich-Alexander-Universität Erlangen-Nürnberg
Energy Campus Nürnberg
Fürtherstraße 250, 90429 Nürnberg, Germany

T. Hrbek, I. Matolínová
Faculty of Mathematics and Physics
Department of Surface and Plasma Science
Charles University
V Holešovičkách 2, Prague 180 00, Czech Republic

R. Grizfeld, Z. Liu, M. Sotome, T. Kondo
Department of Materials Engineering
School of Engineering
University of Tokyo
Bunkyo, Tokyo 113-8656, Japan

unlocks electronic properties and device functionalities that are unattainable through alternative methods.[6]

Compared to conventional semiconductors, for which epitaxial growth is well established, the application of this technique to metal-halide perovskite semiconductors presents unique challenges. The greatest developments in lead-halide perovskites have been realized in photovoltaics, where thin-film solar cells based on polycrystalline materials have reached record power conversion efficiencies, comparable to those of single-crystalline silicon devices. Remarkably, a record power conversion efficiency of 26.7% has been reported for these cells.[7] The advantages of polycrystalline perovskite solar cells stem not only from their cost-effective production via simple solution processing methods but also from their ability to effectively passivate defect states at grain boundaries and surfaces, which would otherwise act as nonradiative recombination sites for free charge carriers.[8–10,11]

In contrast, epitaxially grown perovskite structures have only sparingly demonstrated their potential in optoelectronic applications, despite exhibiting defect densities comparable to those of single-crystal counterparts—ranging as low as $10^9$ $cm^{-3}$, which is up to nine orders of magnitude lower than in polycrystalline films.[12] Flexible single-crystal devices were for instance demonstrated by a solution-based lithography-assisted epitaxial-growth-and-transfer process. Among the devices demonstrated by this process were solar cells based on lead–tin-gradient structures with an average efficiency of ≈19%.[13] Beyond their photovoltaic applications, lead-halide perovskites show considerable promise for X-ray[14] and gamma-ray detection,[15] specifically in the form of single-crystal direct converters. The exceptional performance of lead-halide perovskite single crystals, including their ultra-high sensitivity and ultra-low detection limits, is highly dependent on proper surface passivation.[16,17]

Despite its proven importance in perovskite solar cells[11,18,19] and single-crystal devices,[20–22] surface passivation remains largely unexplored for epitaxial perovskite structures. Numerous studies have introduced epitaxial growth of various metal-halide perovskites on different substrates via commensurate[23–26] or incommensurate[25,27–29] growth techniques, including molecular beam epitaxy,[30] vapor phase deposition,[25,27,28,31–35] and solution epitaxial growth.[13,23–25,36–41] However, the surfaces of these structures have consistently remained un-passivated. Similarly, passivation was omitted in studies demonstrating functionalities such as luminescence from platelets,[31] photodetector response,[25] lasing,[31,42] and quantum coherence[26] in epitaxial films. This omission may stem from the assumption that the smooth and flat surfaces produced by epitaxial growth inherently lack defect states, rendering surface passivation unnecessary.

In this study, we demonstrate the critical role of surface passivation in enhancing the performance of epitaxial lead-halide perovskites across various structural forms, whether synthesized via vapor deposition or solution epitaxy. Our investigation focuses on the optical properties of these structures, specifically photoluminescence (PL) intensity and lifetime, laser thresholds in optical micro-resonators, and specific detectivity in photoconductors. In all cases, surface passivation yields important improvements, underscoring its importance for both smooth and corrugated epitaxial surfaces. These findings establish surface passivation as a pivotal strategy for maximizing the potential of epitaxial perovskite structures, whether through the techniques presented here or by employing alternative passivating molecules and methodologies.

## 2. Surface Passivation of Epitaxial Lead-Halide-Perovskite Micro- and Nanostructures

### 2.1. Surface Passivation of Solution Epitaxial $FAPbBr_3$ Microcrystals to Improve Luminescence Properties

Surface passivation has been extensively shown to noticeably enhance the performance of metal-halide-based optoelectronic devices[43–47] and is particularly critical for improving the stability of unencapsulated solar cells.[48] Consequently, a variety of strategies have been developed for the surface passivation of metal-halide perovskites, including the deposition of cations, anions, Lewis acids, Lewis bases, and wide-bandgap semiconductors.[46] These approaches address the diverse defects that cause carrier trapping or act as recombination centers. Among the numerous passivating agents available, this study focuses on two: TOPO and PMMA. TOPO was chosen due to its established role as a surface ligand in colloidal quantum dot chemistry[49–51] and its demonstrated efficacy in passivating lead-halide perovskites. For instance, DeQuilettes et al. showed that TOPO treatment elevated the photoluminescence quantum yield (PLQY) of perovskite thin films by nearly an order of magnitude and extended the photoluminescence lifetime to 8 µs under solar-equivalent carrier densities.[52] Similarly, Lutao et al. demonstrated that an ultrathin PMMA layer markedly improved carrier lifetimes and mitigated surface defects in $CsPbBr_3$-based Light-Emitting Diodes.[53]

In addition to these findings, PMMA has been shown to refine the photovoltaic performance and stability of solar cells,[54] the photoluminescence of Ruddlesden-Popper perovskites,[55] and the near-infrared amplified spontaneous emission of Methylammonium lead iodide.[56] Nonetheless, these studies primarily address polycrystalline films, which inherently exhibit high defect densities. By comparison, the potential of TOPO and PMMA

Z. Liu, M. Sotome, T. Kondo
Research Center for Advanced Science and Technology
University of Tokyo
Meguro, Tokyo 153-8904, Japan
K. Forberich, C. J. Brabec
Helmholtz-Institute Erlangen-Nürnberg (HI ERN)
Immerwahrstraße 2, 91058 Erlangen, Germany
J. Korczak, A. Szczerbakow, T. Story
Institute of Physics
Polish Academy of Sciences
Aleja Lotnikow 32/46, Warsaw 02–668, Poland
J. Korczak, T. Story
International Research Centre MagTop
Institute of Physics
Polish Academy of Sciences
Aleja Lotnikow 32/46, Warsaw 02–668, Poland
M. Kot, M. A. Loi
Zernike Institute for Advanced Materials
University of Groningen
Nijenborgh 3, Groningen 9747AG, The Netherlands
J. Mergheim
Institute of Applied Mechanics
Friedrich-Alexander-Universität Erlangen-Nürnberg
Egerlandstrasse 5, 91058 Erlangen, Germany

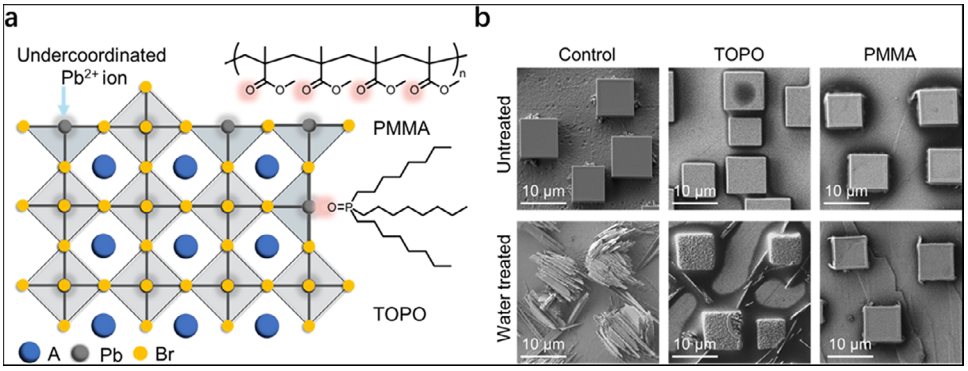


**Figure 1.** Passivation mechanism and water barrier effect of the organic molecular layer. a) Imperfections in perovskite crystals arise from undercoordinated lead ions, and organic molecules such as PMMA and TOPO donate lone pairs of electrons from their oxygen atoms to passivate these defects. b) The first row of SEM images shows perovskite microcrystals without passivation, as well as those passivated with TOPO and PMMA, respectively, while the second row of SEM images corresponds to the microcrystals after dipping the crystals into water.

as passivating agents for epitaxially grown perovskite microcrystals, which may exhibit fewer surface defects due to epitaxial growth, remains largely unexplored. This study investigates the effectiveness of these Lewis bases for passivating various epitaxial lead-halide perovskite microstructures, including laser micro-resonators of $FAPbBr_3$ grown via solution epitaxy and photoconducting wire networks of $CsPbBr_3$ fabricated by vapor phase epitaxy. As illustrated in **Figure 1**a, the C═O and P═O functional groups serve as passivating species by donating lone electron pairs from their oxygen atoms to undercoordinated $Pb^{2+}$ ions, thereby restoring the stoichiometric charge balance of the imperfect surfaces.

The growth of the microcrystal arrays by drop casting with well-controlled shapes is surprisingly robust with respect to conditions, but high luminescence yields cannot be obtained when the growth is performed at high humidity, such as is given on rainy days in a lab with not air condition. Changing temperature simply changes size distributions, and changing molar content changes also the micro-crystallites sizes. Uniform crystal growth over the substrate is always obtained when the deposited precursor droplet is spilling over the sample edges and the solution covers the whole substrate. More critical is the quality of the substrate – it has to be a freshly cleaved from a bigger single crystal and all residuals (powders) have to be carefully removed, making use of isopropanol. Most important is the activation of the substates surface by a 0.125% mass concentration of bromine/methanol solution, which is performed for 5 s with a freshly prepared solution. This solution should always be kept in a tightly closed glass, because it changes composition immediately when opened, and it loses its surface activation activity with proceeding decomposition. It can be used for longer times, however, in when already aged the treatment times have to be prolonged.

To demonstrate the significance of surface passivation, we first examined epitaxially grown micro-resonators functioning as optically pumped lasers. These micro-resonators, characterized by their simplicity and high reproducibility, are fabricated via solution epitaxial growth. Specifically, nearly perfectly cuboidal $FAPbBr_3$ micro-resonators, epitaxially grown on lead sulfide (PbS) substrates, were produced through drop-casting, with their dimensions governed by the precursor concentration.[57] In terms of lasing performance, alternative deposition techniques, such as epitaxial growth by antisolvent vapor-assisted crystallization, can achieve up to a 30% reduction in threshold pump powers, albeit at the expense of obviously longer growth times.[57] For this work, precursors were selected to yield micro-resonators with lateral dimensions below 10 μm (Figure 1b, top-left panel), which are optimal for achieving low lasing thresholds.[57]

To passivate the surfaces, the epitaxial microcrystals were coated by spin-coating a 10 mg $mL^{-1}$ TOPO solution or a 2.5 mg $mL^{-1}$ PMMA solution in toluene. Following solvent evaporation, scanning electron microscopy (SEM) revealed TOPO ligands or PMMA as dark regions around the perimeters of the micro-resonators or, occasionally, as dark spots on their top surfaces. In most areas, though, no distinct signatures of the deposited materials were visible under SEM (Figure 1b, top-middle and top-right panels). To confirm the presence of organic passivating agents on the surfaces, we conducted a controlled water immersion test. Unprotected $FAPbBr_3$ microcrystals were immersed in water for one second and then dried with compressed air, resulting in apparent morphological changes. The cuboidal crystals were effectively destroyed, decomposing into needle-like sheets that partially aligned, resembling lamellas in a closed jalousie. This transformation is attributed to the dissolution of organic ammonium salts in the perovskite lattice.

By comparison, microcrystals treated with TOPO exhibited strengthened resistance to water. Although some needle-like structures formed around the cuboids and minor surface corrosion was observed, the micro-resonators largely retained their initial shapes and dimensions. This pronounced difference emphasizes the hydrophobic and protective properties of TOPO on the $FAPbBr_3$ surfaces. Even greater stability was accomplished with PMMA passivation. The spin-coated PMMA layers effectively shielded the crystal surfaces, showing virtually no signs of etching after immersion. The superior protective efficacy of PMMA compared to TOPO may arise from the higher Lewis basicity of the oxygen atom from the carbonyl group along its polymer backbone compared to the oxygen atom from TOPO, which forms stronger and more persistent bonds than TOPO's single P═O electron pair. To explore whether the enhanced water resistance observed with PMMA also translates into superior optical

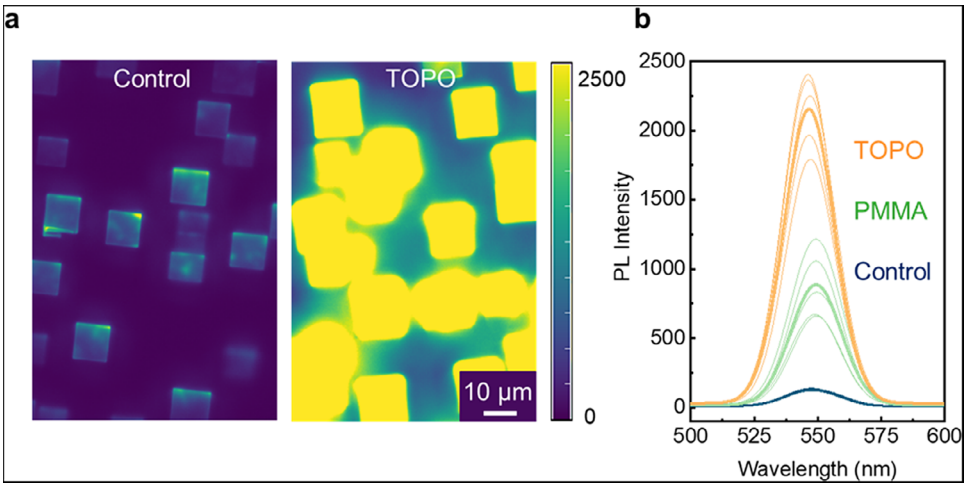


**Figure 2.** Effect of surface passivation on micro-luminescence of epitaxial $FAPbBr_3$ microcrystals. a) Photoluminescence maps of the $FAPbBr_3$ microcrystals without passivation (left) and passivated by 10 mg $mL^{-1}$ TOPO/toluene. b) Photoluminescence (PL) spectra for 15 microcrystals from the three types of samples, untreated, TOPO, and PMMA-passivated $FAPbBr_3$ microcrystals. The lines in bold represent the averaged spectra for each sample type.

passivation, we investigate the optical properties in the subsequent section.

To evaluate the passivation effects of TOPO and PMMA on perovskite microcrystals, hyperspectral PL microscopy and time-resolved photoluminescence (trPL) measurements were conducted. It should be noted that the luminescence properties of lead-halide perovskites are sensitive to aging and environmental factors, particularly light exposure during experiments—a well-documented phenomenon in these materials. To ensure accurate and consistent comparisons, all samples were prepared one day prior to the experiments and stored under identical conditions. Measurements were completed within five minutes for each sample.

For both passivated and pristine microcrystals, emission spectra were recorded, exhibiting a single peak near 548 nm, consistent with $FAPbBr_3$ single crystals.[58] All PL spectra were measured under the same conditions (integration time of 0.5 s), enabling direct comparison across samples. Un-passivated microcrystals exhibited weak and uneven emission, as reflected in the photoluminescence maps (**Figure 2a**). This uneven intensity distribution is attributed to the irregular surface of manually cleaved substrates, which often caused individual microcrystal surfaces to fall slightly out of focus under the optical microscope.

In stark contrast, TOPO-passivated microcrystals emitted with considerably greater intensity, leading to blurred images where adjacent microcrystals appeared to merge into connected regions (Figure 2a, right panel and Figure S1, Supporting Information). For a quantitative comparison, the integrated intensity of each microcrystal was calculated over a 10 μm × 10 μm area, as outlined in the white squares of the intensity maps (Figures S1–S3, Supporting Information). To statistically validate the results, 15 microcrystals of comparable size (≈12 μm) were randomly selected from the reference and passivated samples. The TOPO-passivated samples exhibited a more than tenfold increase in luminescence intensity compared to the reference, demonstrating that TOPO effectively suppresses nonradiative recombination by passivating surface defect states (Figure 2b). TOPO represents an L-type ligand, acting as Lewis base, which binds to electron-deficient surface cites. Fourier transform infrared experiments combined with X-ray photoelectron spectroscopy (XPS) proved that the electronegative oxygen of P═O forms bonds to $Pb^{2+}$/metallic Pb,[59] which are present at the surface of the $FAPbBr_3$ crystals, Figure 1a. These bonds passivate the surface trap states.

PMMA, which has shown superior water protection ability for the $FAPbBr_3$, Figure 1b, exhibits basically the same passivation effects as TOPO, in this case via the electronegative C═O. By XPS performed on single crystalline $CsPbBr_3$ films it was shown, for instance, that passivation by PMMA results in elimination of uncoordinated metallic Pb atoms from its surface.[53] The achieved passivation decreases the non-radiative recombination and results in a decreased photoluminescence line width, due to reduced disorder in the energy states close to the and gap. Basically, the same happens on the epitaxial $FAPbBr_3$ crystallites (Figure 2b). The PMMA-covered samples show a luminescence peak intensity that is increased by a factor of ≈5, while for the TOPO passivated sample, the luminescence-increase amounts to a factor of 15.

To quantify the PL quantum yield from the passivated $FAPbBr_3$ microcrystals we compared their micro-luminescence maps with those of a well-characterized reference sample. The reference consists of colloidal $CsPbBr_3$ nanocrystals synthesized according to the procedure described in ref. [60] embedded into a PMMA matrix (inset in **Figure 3a**). For a thick film of these nanocrystals in PMMA blend, we measure a PLQY of 72% (Figure 3a) with an integrating sphere. A direct comparison of the microluminescence spectra extracted from the hyperspectral microscopic PL provides 22% of the intensity of the reference for the TOPO passivated microcrystals (Figure 3b,c). This lower emission intensity is caused to a great part by a reduced outcoupling efficiency, rather than by a strongly reduced radiative recombination rate. We estimated the difference in outcoupling efficiency between the epitaxial microcrystals by considering the angle-dependent transmission coefficient for internal reflection at an interface between

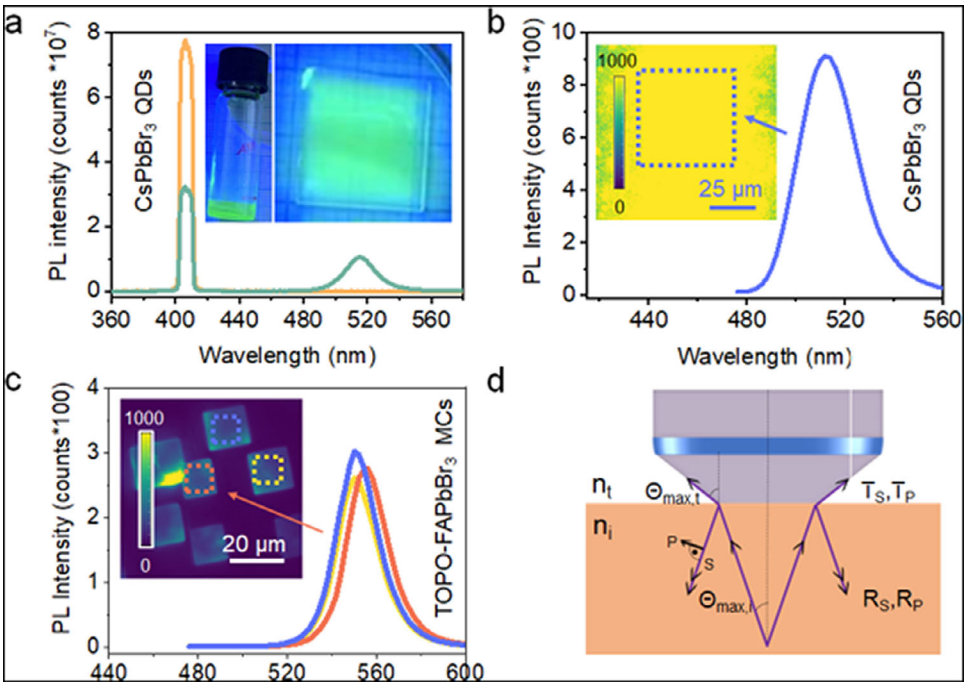


**Figure 3.** Quantum yield of individual epitaxial $FAPbBr_3$ microcrystals. The quantum yield was determined by comparison with a well-calibrated reference sample, $CsPbBr_3$ nanocrystals in PMMA matrix. a) Quantum yield measurement in an integrating sphere of the reference sample (sample is shown as an inset in the solution form and as a deposited film on glass). The orange line represents the laser excitation without sample, and the green line represents the emission of the nanocrystals and the rest of the laser emission. b) Hyperspectral photoluminescence microscopy image and luminescence spectrum of the reference. c) Hyperspectral photoluminescence microscopy image and luminescence spectra of the TOPO-protected $FAPbBr_3$ epitaxial microcrystals measured under identical conditions. Further spectra are given in Figure S5 (Supporting Information). d) Sketch of the luminescence cone of emission that can be collected by an objective with a numerical aberration of 0.8.

a medium with $n = 2.37$ (representing perovskite) or $n = 1.49$ (representing PMMA) and air, using the angle-dependent Fresnel formulas (details are given in Supporting Information). The emission into the whole solid angle (Figure 3d; Figure S4, Supporting Information) was considered by discretizing the angle between 0° and 90° and computing the transmission coefficient separately for each angle. The overall transmission value was obtained by integrating over all angles, taking into account the solid angle and the cosine projection. Finally, we considered that only photons emitted into a certain angle were measured since the emission was collected with a lens with a numerical aperture of 0.8. As a result, we find that 4.8% of total emission is coupled out for $n = 2.37$ (with a maximum internal emission angle of 19.7°), and 14.9% of total emission is coupled out for 1.49 (with a maximum internal emission angle of 32.5°). This results in a factor of 3.1 between the outcoupling coefficient of PMMA and $FAPbBr_3$, which is based only on the difference between reflection and transmission coefficients. Taking these different coupling efficiencies into account, the quantum yield of the $FAPbBr_3$ microcrystals is ≈68% of that of the colloidal nanocrystal reference providing a PLQY value of 49%, is considerably lower than what is achieved in $FAPbBr_3$ colloidal nanocrystals, reporting values between ≈70% and 95%,[61] but is considerably higher as in $FAPbBr_3$ based thin films, with measured PLQY of ≈0.5% for a pristine film. Only when $FAPbBr_3$ is doped by Cerium the quantum yield is increased to exceed 10%.[62]

Surface passivation not only affects the PL intensity but also its transient behavior, which is affected by several recombination mechanisms either in sequence or in parallel, combined with excess charge carrier diffusion. To get a consistent picture here a rate equation model was considered, which was previously successfully applied to determine the trap density in a polycrystalline $CsPbBr_3$ film prepared by aerosol deposition.[63] The rate equation model considers direct band-to-band recombination by a rate $k_{bb}$, and recombination via trap states via trap and release coefficients $k_t$ and $k_r$. The rate equation model, which is described in the supporting information of ref. [64] is suitable for thin films for which carrier diffusion effects are usually neglected, assuming an instantaneous homogenization of the excess charge carriers over the film cross sections. While this assumption is justified for thin films, in the present case of epitaxial microcrystallites with thicknesses in the 10 µm range, the photoluminescence quenching due to diffusion has certainly to be considered. Thus, we added a diffusion term to the rate equation from ref. [64], which is proportional to the second derivative of the excess charge carrier concentration times the diffusion constant: $D\frac{\partial^2 \delta n}{\partial x^2}$. The rate equation, solved by a finite element approach, allowed to differentiate trap densities at the surface, within the bulk of the sample, and at the bulk/substrate interface, by parameters $N_{ts}$, $N_{tb}$, $N_{ti}$. Comparisons with experiments were then done by assuming that the measured luminescence is proportional to the excess charge carrier concentration present at the top-most

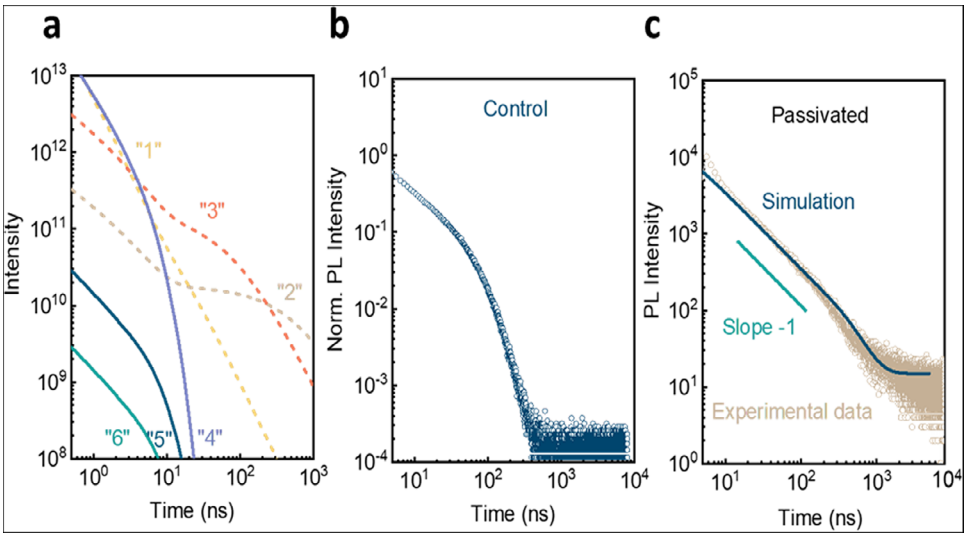


**Figure 4.** Effect of passivation on the transient photoluminescence of epitaxial $FAPbBr_3$ microcrystals. a) Simulation results from a drift diffusion model for various sets of parameters. 1,2,3 varies the band-to-band recombination rate for small diffusion and does not consider any carrier trapping. 4,5,6 considers trap states at the surface and at the perovskite/substrate interface. If diffusion is dominant the initial slope is −1. b) Time-resolved PL transient of untreated $FAPbBr_3$ microcrystals for an excitation intensity of 617 nJ $cm^{-2}$. c) Transient PL measured for a fluence of 617 nJ $cm^{-2}$ for $FAPbBr_3$ microcrystals passivated by 2.5 mg $mL^{-1}$ PMMA/ toluene. The solid curve represents simulated results, providing a best fit to the data assuming diffusion and trap assisted recombination at the perovskite-substrate interface only.

element of the model located at the sample surface. Conversely, all excess charge carriers were assumed to be generated by a short laser pulse within this topmost surface element. Thus, excess charge carriers diffusing away from the surface do not contribute to the detected luminescence. **Figure** 4a summarizes the most relevant of the simulation results. As example, the effect of band-to-band recombination rate at constant diffusion ($D = 2.5 \times 10^9$ µm$^2$ s$^{-1}$) was simulated by changing $k_{bb}$ ($1 \times 10^2$ µm$^3$ s$^{-1}$ for ("2"), $1 \times 10^3$ µm$^3$ s$^{-1}$ ("3"), and $1 \times 10^5$ µm$^3$ s$^{-1}$ ("1") without considering any trap states. What can be seen from this comparison is for instance for high band recombination coefficients ($k_{bb}$, "1") there is a short decay time and there is almost no influence of diffusion. In contrast, for small $k_{bb}$ ("2") a fast decay until ≈20 ns due to band-to-band recombination is followed by a slower decay, caused by diffusion. If now trap states are added at the surface and at the interface in between the perovskite and the lead sulfide substrate (with densities $N_{ts} = 1 \times 10^5$ µm$^{-3}$, and $N_{ti} = 1 \times 10^7$ µm$^{-3}$, respectively with $k_t = 1 \times 10^4$ µm$^3$ s$^{-1}$, $k_r = 1 \times 10^2$ µm$^3$ s$^{-1}$) then drift and diffusion ("4", $k_{bb} = 1.0 \times 10^4$ µm$^3$ s$^{-1}$, $D = 5 \times 10^9$ µm$^2$ s$^{-1}$) cause an initial slope of the excess charge carrier density to be in between −1 and −2. Only when the band-to-band recombination is small, and diffusion is high ("5", $k_{bb} = 10$ µm$^3$ s$^{-1}$: $D = 5 \times 10^9$ µm$^2$ s$^{-1}$ and "6", $k_{bb} = 1$ µm$^3$ s$^{-1}$, $D = 5 \times 10^9$ µm$^2$ s$^{-1}$) the initial slope is −1 due to diffusion and decreases significantly after ≈10 ns, which is caused by trap-assisted recombination at the perovskite/substrate interface.

Having these simulated results in mind, it is straightforward to interpret the results from the transient photoluminescence experiments for the control sample, presented in Figure 4b. These data were measured with an excitation fluence of 627 nJ $cm^{-2}$ to achieve a good signal to noise ratio. The transient shows an initial slope of −1 up to ≈70 ns, which is according to the simulations indicates a diffusion-limited luminescence decay, whereas after this time the slope becomes much steeper, close to −3. This steep luminescence decrease cannot take place without significant contributions from trap assisted recombination, and for the reference sample it causes the luminescence to vanish after ≈400 ns. This is in contrast with the transient photoluminescence measured for the PMMA passivated sample (Figure 4c) for which a considerably longer luminescence decay was observed, persisting for at least 1 µs under identical excitation conditions. Indeed, the experimental transient fits well to a simulated one, obtained for the following set of parameters: $D = 1 \times 10^8$ µm$^2$ s$^{-1}$; $k_t = 1 \times 10^3$ µm$^3$ s$^{-1}$; $k_r = 0$; $k_{bb} = 0$; $N_{ts} = N_{tb} = 0$; $N_{ti} = 1 \times 10^5$ µm$^{-3}$. The set of parameters basically predicts that the luminescence is diffusion limited and affected only by interfacial recombination, causing the slope to slightly become steeper after ≈200 ns. Adding recombination in the bulk or trap-assisted recombination at the surface will always provide a steeper initial slope. That the interfacial recombination cannot be avoided is clear, because of the by far smaller bandgap energy of the PbS substrate than that of the $FAPbBr_3$ microcrystals. It should be noted that the diffusion constant determined by the fit of 1 cm$^2$/s can be converted into a mobility $\mu\epsilon = 38$ cm$^2$ Vs$^{-1}$ by making use of the Einstein relations ($D/\mu = k_B T/e$, with $k_B$-Boltzmann constant, $T$-temperature, and $e$-elemental charge). This value is higher than that achieved by the band like transport in quantum-dot based transistors with ultrahigh detectivity[65] with a hole mobility of 14 cm$^2$ Vs$^{-1}$, but is smaller than in $FAPbBr_3$ single crystals for which a trap-free hole mobility was determined by Mott–Gurney's space charge limited current theory from the Child region, providing ≈200 cm$^2$ Vs$^{-1}$.[66] This high value for the single crystal was achieved after a trap passivation treatment by exposure of the crystals to UV-$O_3$.

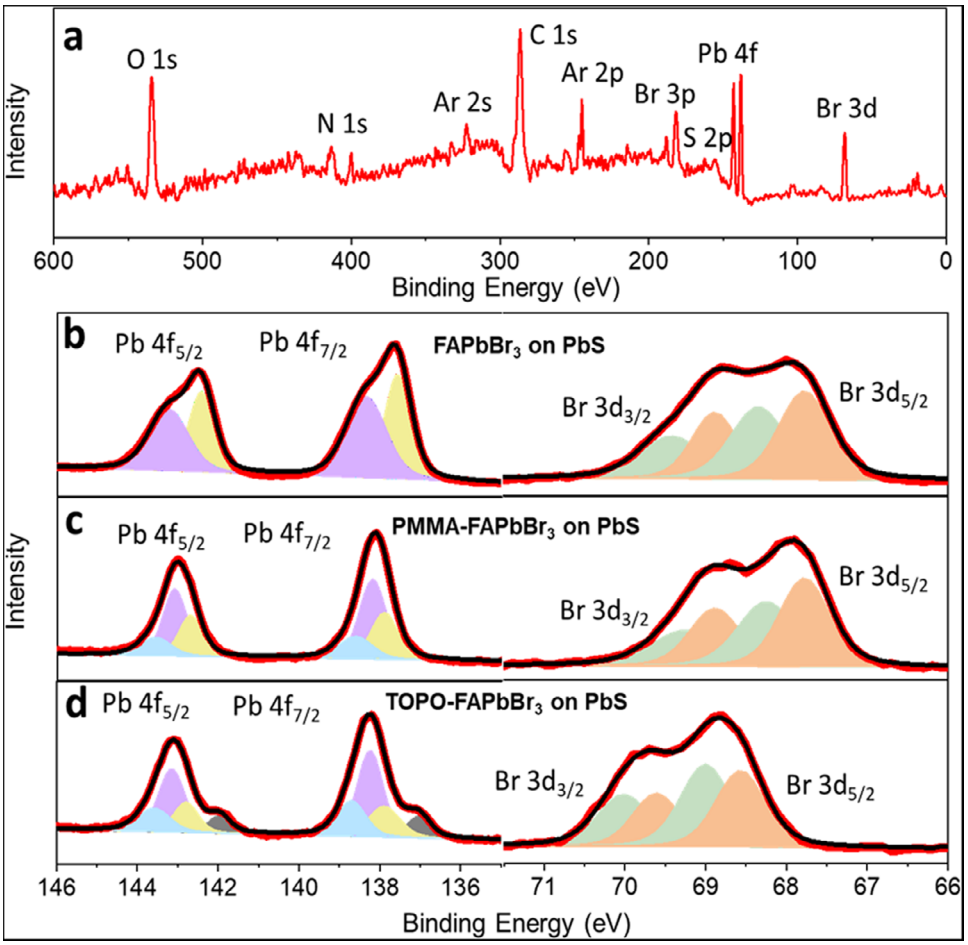


**Figure 5.** Near-ambient-pressure X-ray photoelectron spectroscopy of $FAPbBr_3$ epitaxial microcuboids on PbS. a) Survey spectrum for PMMA-covered $FAPbBr_3$/PbS showing all expected elements. b–d) Details of the Pb 4f and Br 3d peaks for the uncovered sample and samples covered by PMMA and TOPO. The fitted peaks are color-coded for different bond configurations as follows: Pb-Br in $FAPbBr_3$ (orange) and in PbBr (bright green), Pb-S (yellow), Pb-Br (violet), Pb-O (light blue), metallic $Pb^0$ (grey). The corresponding peak positions are provided in Tables S1 and S2 (Supporting Information).

### 2.2. Quantifying Surface Passivation of $FAPbBr_3$ by PMMA and TOPO

To prove the higher environmental protection ability of PMMA in respect to TOPO in a quantitative way, XPS is applied. Since the surface adsorbed passivating agents can be removed when the samples are inserted into an ultra-high vacuum (UHV), we have chosen to perform near-ambient-pressure (NAP) XPS in Ar-atmosphere with a pressure of 1 mbar, rather than UHV-XPS. The survey NAP-XPS spectrum of the PMMA-protected $FAPbBr_3$/PbS sample exhibits all expected elements, as indicated in **Figure** 5a. The C1s peak, which is usually used as a well-known reference point, in this case it is more involved, since on the nominally carbon free PbS sample a carbon is found from contaminant which is possibly present also on all other samples, for PMMA at least five carbon peaks are found due to carbon atoms present in different pond configurations such as O—C═O, COO—, C—O, C—C═O, C—C/C—H,[67] and the carbon peak from the formamidinium is possibly shifted by surface passivation. Using the C 1s peaks for calibration of the energy scale can be imprecise to compensate for shifts of the energy scale due to sample charging, especially considering that reported peak-shifts originating from passivation of lead-halide perovskites reported in literature are in the order of ≈0.2 eV or even smaller.[67–72,73] Thus, we present the XPS data on uncorrected scales, except when explicitly stated. Since the $FAPbBr_3$ epitaxial microcrystals only partly cover the PbS substrate, the first step is to understand the substrate, both without and with passivating species. The pristine PbS substrate exhibits a characteristic Pb $4f_{7/2}$ and $4f_{5/2}$ double peak that is found at binding energies 137.4 and 142.2 eV due to the Pb—S bonds, with small shoulders towards higher energies indicating the presence of small amounts of surface PbO (Figure S6a, Supporting Information), at energies of 138.1 and 142.9 eV, in close agreement with ref. [74] As listed in Table S1 (Supporting Information), after deposition of PMMA and TOPO, the Pb 4f peaks due to the Pb—S bonds shift to higher energies by 0.2 eV, indicating a changed binding energy due to charging. Nevertheless, the Pb—O shows larger shifts after deposition of PMMA and even larger ones after deposition of TOPO (Figure S6b,c and Table S1, Supporting Information). Without charging effect, the PMMA forming Pb—O═C, Pb—O—$CH_3$ resonant moieties, shift the Pb—O peak by 0.2 eV, and the TOPO, reacting on

the surface via Pb—O=P, shifts the Pb—O by 0.3 eV, with respect to the native P—O (presumably from PbO, or hydrated PbO). Considering the areas of the peak, the fraction of Pb-O increased from the native PbS (12% with respect to Pb—S) to the PMMA (25%) and TOPO (27%).

The deposited $FAPbBr_3$ on PbS causes a by far more drastic change of the Pb 4f spectra as the oxidation by the passivating agents does. In particular, another 2 significant NAP-XPS peaks appear on the high energy side of the Pb-S peaks (yellow) due to Pb-Br (bright blue) (Figure 5b; Table S2, Supporting Information) with energies of 138.3 and 143.2 eV, in the range to those reported for $FAPbBr_3$ polycrystalline films.[75,76] The Pb-Br peaks are located between the Pb-S and the Pb-O peaks. For this sample, the Br 3d exhibits a doublet ascribed to $3d_{5/2}$ and $3d_{3/2}$[77] that always obeys an intensity ratio of 3:2. To fulfill that intensity ratio, the NAP-XPS spectra due to Br between 67 and 71 eV have to be fitted by two double peaks. The low-energy doublet with ≈1 eV splitting (orange in Figure 5b) corresponds to Br in $FAPbBr_3$[78] and the higher energy doubled (bright green) to that of Br in $PbBr_2$,[79] resulting from a partial removal of the formamidinium molecules at the $FAPbBr_3$ surface (Table S2, Supporting Information). These 4 Br peaks do not shift at all, by deposition of PMMA, so that we consider no charging effects for this sample. The Pb 4f spectra for the PMMA-covered sample, exhibits for the Pb $4f_{7/2}$ only a single peak, even though we know that there should be Pb—S bonds from the substrate, Pb—Br bonds from the $FAPbBr_3$ as well as Pb—O due to the PMMA passivation. In order to deconvolute these three contributions, we allowed only small shifts for all peaks, with respect to that obtained for the non-passivated sample (Pb—S, Pb—Br) or for the PMMA passivated PbS substrate (Pb—O), resulting in a Pb—O to Pb-Br ratio of 35%. The TOPO-passivated sample, first of all shows a downshift of the Br 3d peaks by 0.7 eV. Since the Br should not be much affected by the oxygen bond of the passivating agents to the surface Pb atoms, this collective shift we attribute to a charging effect, which we thus removed from the Pb 4f peaks. Furthermore, for deconvolution, the same peak energies were then applied as for the PMMA-covered sample, resulting in a somewhat higher Pb-O to Pb-Br ratio of 44%. In this spectrum (Figure 5c), an additional peak appeared on the lower energy side of the Pb-S peak, which can be attributed to metallic $Pb^0$, which was most probably formed due to extensive X-ray excitation in the charging sample. Thus, in total, the NAP-XPS analysis suggests a somewhat more complete passivation of the $FAPbBr_3$ by TOPO than by PMMA, which is in agreement with the optical characterization of the samples described in the following.

### 2.3. Surface Passivation of Solution Epitaxial $FAPbBr_3$ Microcrystal Lasers

To assess the impact of surface passivation at high excess carrier densities, we examined its effect on the lasing properties of $FAPbBr_3$ microcrystals under 1.3 ns-pulsed excitation at a wavelength of 532 nm. All experiments were conducted under ambient conditions, and the emission was excited and collected through the objective of an optical microscope. To protect the perovskite microcrystals from laser damage and ensure accurate threshold measurements, each sample was exposed to the focused laser beam for no more than 10 min. Solution-grown epitaxial $FAPbBr_3$ micro-resonators have previously demonstrated high lasing stability under ambient conditions.[80] Among halide-perovskite micro-resonators, only $CsPbBr_3$ exhibited superior stability, but this superior laser stability was observed exclusively in inert nitrogen atmospheres.[80]

Recent advancements in $FAPbBr_3$ micro-resonators, achieved through epitaxial growth using antisolvent vapor-assisted crystallization, have optimized the lasing threshold to 66 kW $cm^{-2}$ at a repetition rate of 1 kHz.[57] For samples produced by drop-casting, which we use here due to its simplicity and high reproducibility, the average threshold power was found to be close to 100 kW $cm^{-2}$, with the lowest recorded threshold power being around 90 kW $cm^{-2}$.[57] The excitation intensity-dependent spectra reveal a clear transition: from broadband spontaneous emission with a peak at 552 nm and a full width at half maximum (FWHM) of ≈17 nm at low excitation intensities, to the emergence of a narrow emission peak (≈0.8 nm, limited by spectrometer resolution) superimposed on the spontaneous emission maximum just above the threshold, and finally to a dominating narrow peak at high excitation powers (**Figure 6a**). This lasing threshold is highly reproducible, in that we found almost identical results for very similar sized individual microcrystals grown on different substrates (Figures S7 and S8, Supporting Information). For the given $FAPbBr_3$ micro-resonators, the spontaneous emission is noticeably weaker than the stimulated emission, making the characteristic linewidth narrowing at the threshold most apparent when spectra are displayed on a logarithmic scale (Figure 6a). TOPO-passivated samples, shown in Figure 6b on a linear scale, also exhibit a pronounced narrow lasing peak above the threshold. At high excitation powers, the spontaneous emission background becomes visible but is dominated by the lasing signal.

To determine accurate laser threshold values, the spectrally integrated intensity was plotted against the pump power on a log-log scale (Figure 6c). Both TOPO-passivated and reference samples exhibit typical S-shaped dependencies, highlighted with linear fits as guides for the eye. The comparison of these curves points out the greatly optimizations completed through surface passivation. The passivated samples exhibited higher integrated intensities at all pump powers and a critically reduced lasing threshold. Even the reference sample, with a threshold of 86 kW $cm^{-2}$, outperformed previously reported values for drop-cast epitaxial lead-halide perovskites. Remarkably, the TOPO-passivated sample achieved a threshold of 29 kW $cm^{-2}$, nearly three times lower than the reference and the lowest lasing threshold ever reported for an epitaxial microcavity laser structure based on lead-halide perovskites and measured with a pulsed laser with a repetition rate in the kHz range. (see Table S3, Supporting Information for a comparison of laser thresholds from various epitaxial metal halide perovskite structures reported in literature). Lower threshold values have only been obtained for square-shaped lead halide perovskite laser resonators, when they are pumped with substantially lower repetition rates of 100 Hz or even 10 Hz (see Table S4, Supporting Information), for which device cooling between laser pulses is greatly facilitated. The obtained threshold values depend on details of the passivation procedure and are worse when the recipe deviates from the optimum TOPO concentration of 10 mg $mL^{-1}$ in toluene, as shown

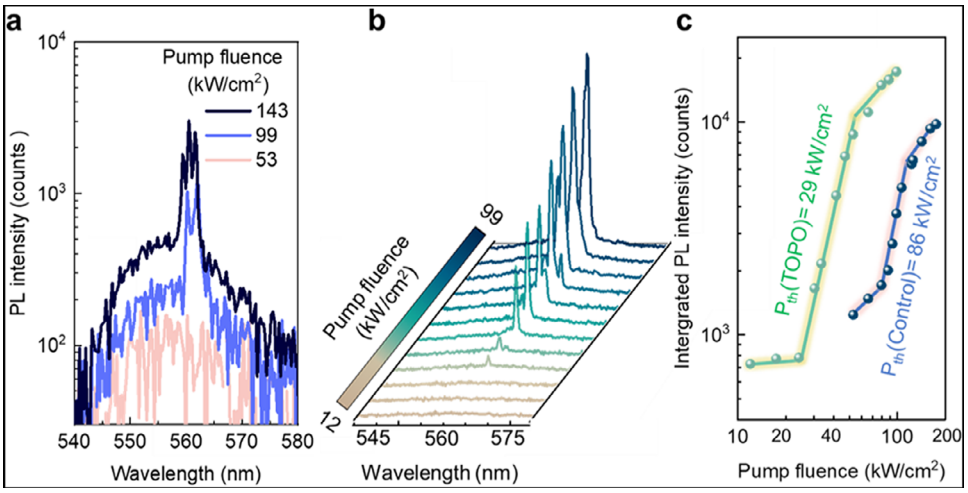


**Figure 6.** Effect of surface passivation on lasing of cubic-shaped $FAPbBr_3$ micro-resonators. a) Excitation intensity-dependent spectra of an un-passivated single $FAPbBr_3$ microcrystal with a length of ≈7 µm. Excitation was conducted at 532 nm with 1.3 ns long pulses. b) Laser emission of a single $FAPbBr_3$ microcrystal passivated with 10 mg $mL^{-1}$ TOPO/toluene, with a length of ≈7 µm. Excitation was performed at 532 nm with 1.3 ns long pulses. c) Intensity dependence evaluated from the spectra in Figure 6b and Figure S8 (Supporting Information) at the wavelength of the laser peak.

by the mean threshold values measured for 40 micro resonators in Figure S9a. For PMMA passivation, for which example lasing spectra and threshold curves are demonstrated in Figure S10 (Supporting Information), the optimum concentration is 2.5 mg $mL^{-1}$ (Figure S9b, Supporting Information).

The surface passivation procedures demonstrated above to improve PL quantum yield and lasing thresholds also provide improved long-time stability of the micro-resonators in lasing. As an example, the unprotected $FAPbBr_3$ microcrystals showed a greatly enhanced laser threshold power after storage for two months in a nitrogen-filled glove box followed by a further two months in the ambient. The spectra (**Figure 7a**) show only spontaneous emission up to a pump fluence up to 170 kW $cm^{-2}$, which is the same maximum value for which the spectra are also shown in Figure 7b. The results for the PMMA-protected sample are shown, which allows to observe lasing, however, with an increased threshold power of 106 kW $cm^{-2}$ (Figure 7b) as compared to the freshly grown sample. Interestingly, the PMMA-protected sample showed the same threshold of 106 kW/$cm^2$ also for the freshly prepared sample after water treatment, as is shown in the comparison of 45 micro-resonator thresholds before and after water treatments for three sample types – unprotected, TOPO-treated and PMMA-treated, in Figure 7c. Thus, the surface passivation of epitaxial microstructures results in an increased stabilization in ambient and even in the harsh environment given by immersion in water. While TOPO provides a better passivation for the freshly prepared samples, PMMA provides superior water protection and thus better thresholds for water-treated and aged samples.

### 2.4. Surface Passivation of Epitaxial $CsPbBr_3$ Nanowires From Thermal Evaporation

While we focused up to this point on surface passivation of epitaxial $FAPbBr_3$ structures with micrometer dimensions, surface passivation should have an even more pronounced effect on epitaxial nanostructures, for which the main portion of the material is close to the surface, possibly within the exciton- or free carrier diffusion length from the surface and surface defects. Solution epitaxial growth via drop-casting facilitates the formation of micron-sized, oriented crystallites in a simple and rapid manner. By adjusting the precursor solution concentration, the final dimensions of the microstructures can be partially controlled. However, for fabricating nanometer-scale structures, methods with slower deposition rates may be more suitable, as the dimensions in such cases are primarily governed by deposition time. Vapor-phase deposition methods, which are more commonly employed than solution epitaxy, offer distinct advantages, especially for depositing all-inorganic perovskites.[27,28,31,32,35] These methods enable perovskite evaporation without generating corrosive hydro-halide acids, typically formed as decomposition products of organic-inorganic hybrid perovskites under vacuum conditions. Thus, the epitaxial growth of nanostructures by evaporation was performed for $CsPbBr_3$, which was conducted in an evaporation chamber equipped with a substrate heater, maintained at 375 °C the growth proceeded over a duration of 3 h and was performed on freshly cleaved muscovite mica substrates. The incommensurate van der Waals-type epitaxial growth resulted in a network of well-aligned, surface-bound nanowires. These nanowires were horizontally oriented on the mica (001) surface, and their morphology was characterized using atomic force microscopy (AFM) (inset, **Figure 8a**). The nanowires exhibited varying dimensions, with heights reaching up to 300 nm and widths generally below 1 µm. Notably, the top surfaces displayed crystalline facets devoid of observable defects or imperfections.

In accordance with the literature,[27,28,32,35] many nanowires were parallel, with growth directions exhibiting six-fold symmetry. Angles of 60° or 120° were observed between nearly all interconnected nanowires. Figure S11 (Supporting Information) presents the X-ray diffraction (XRD) patterns of the as-grown samples, compared with the mica substrate and a $CsPbBr_3$ standard. While the mica substrates displayed a series of nearly equally spaced diffraction peaks, the samples exhibited additional

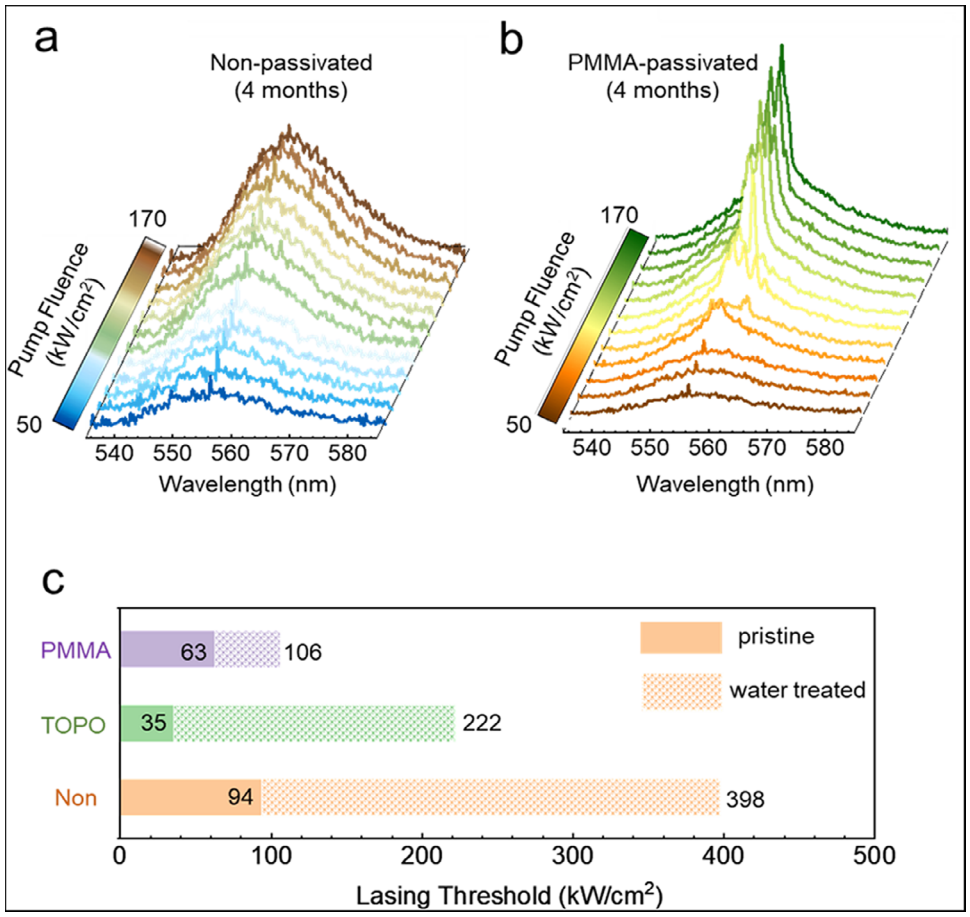


**Figure 7.** Surface passivation maintains lasing in $FAPbBr_3$. a,b) exhibit emission spectra upon sample storage for 2 months in nitrogen and further two months in the ambient for a non-passivated sample and a PMMA passivated one. c) Lasing thresholds measured for surface passivated and non-passivated micro-resonators before and after treatment in water. Shown are averaged values for 45 micro-resonators for each sample type. The passivating agent is given on the left side.

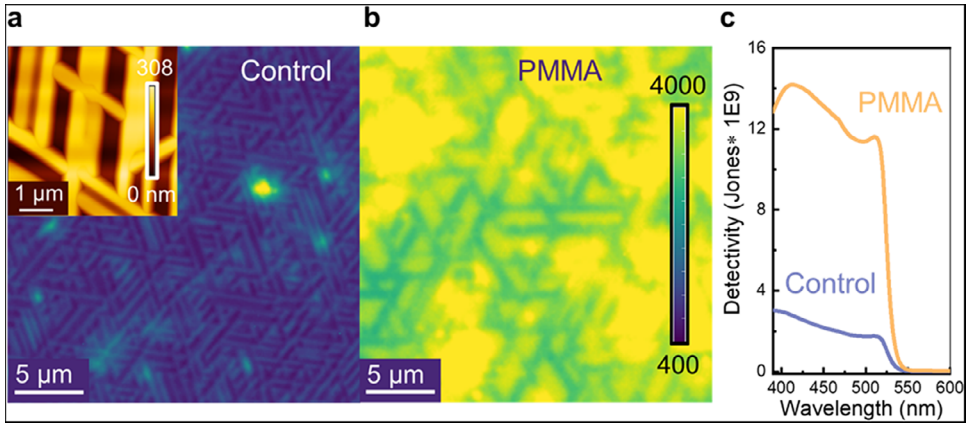


**Figure 8.** The optoelectronic performance of passivated $CsPbBr_3$ nanowires. a) PL map of the non-passivated $CsPbBr_3$ nanowires fabricated by vapor phase deposition methods. The inset displays the AFM topography of the non-passivated $CsPbBr_3$ nanowires. b) PL map of the $CsPbBr_3$ nanowires passivated using a 10 mg $mL^{-1}$ PMMA/toluene solution. c) Specific detectivity spectra of passivated and non-passivated $CsPbBr_3$ nanowires, after the deposition of a thin PMMA layer, the detectivity was greatly increased by a factor of six compared to the control group.

peaks at 21.55° and 44.10°, corresponding to the (110) and (220) planes of cubic-phase $CsPbBr_3$ (space group: $Pm\bar{3}m$, $a = 5.830$ Å). The absence of other $CsPbBr_3$ diffraction peaks strongly suggests that the nanowires were highly oriented, consistent with epitaxial growth, where the (110) lattice planes of $CsPbBr_3$ align parallel to the mica surface.

While the nanowire network exhibits features characteristic of epitaxially grown samples, the varying orientations supported by the mica substrate impart a polycrystalline nature to the overall film. The crystalline wire segments, which are several micrometers in length, are organized into a network with a triangular pattern, as evident in the microscopic PL image of the as-grown sample (Figure 8a). The overall PL intensity of these samples was low, requiring a 10 s integration time to detect emission at each point in the PL map. Apart from a few exceptionally bright spots, the PL image consistently shows bright needle-like structures separated by dark regions corresponding to $CsPbBr_3$ wire emission areas, with uncovered mica regions in between.

Passivating the structures with PMMA did not alter this spatial pattern but resulted in a marked increase in PL intensity across the entire sample area. For the reference sample, the detected luminescence intensities were near the lower end of the intensity scale, starting at ≈400 counts for a 10 s integration time. Following PMMA passivation, the luminescence intensity increased to ≈4000 counts, reaching the upper end of the scale (Figure 8b). At several locations, the emission was so intense that it appeared blurred, obscuring details of the underlying microstructure.

A comparison of the PL maps in Figure 8a,b demonstrates a nearly one order-of-magnitude enhancement in luminescence intensity due to passivation. Importantly, the PL spectra of both passivated and un-passivated samples are identical, as shown in Figure S12 (Supporting Information), and correspond to the bulk $CsPbBr_3$ emission, with a peak at 536 nm.[81] This result confirms that the boosted luminescence arises from reduced nonradiative recombination rather than changes in the material's intrinsic optical properties.

The interconnected network of triangularly arranged nanowires facilitates lateral charge transport through the $CsPbBr_3$ film, rendering it promising for applications such as photoconductive detectors. A critical figure of merit for photodetectors is specific detectivity (D*), which quantifies the device's responsivity relative to the noise current density, normalized by the detector area and bandwidth. It is noteworthy that the $CsPbBr_3$ nanowires do not fully cover the substrate, and their thin structure may limit their ability to absorb all incident photons. As previously discussed, the reference sample exhibits weak luminescence, likely due to surface defects, defects at the perovskite/mica interface, and bulk material imperfections.

Despite these challenges, we successfully measured the responsivity spectrum and noise current to derive the detectivity spectrum, as shown in Figure 8c. The spectrum displays the characteristic feature of vanishing at wavelengths corresponding to the semiconductor's bandgap, while a broad photoconductive response is observed at sub-bandgap wavelengths. Overall, the detectivity is moderate; nevertheless, similar to the photoluminescence, it is highly sensitive to surface passivation. Following the deposition of a thin PMMA layer, the detectivity advanced significantly, comparable to the boost observed in photoluminescence. Across all wavelengths, the detectivity exhibited an improvement by nearly a factor of six, demonstrating the efficacy of PMMA passivation in enhancing the performance of photoconductive devices fabricated via epitaxial growth.

## 3. Discussion

Even though epitaxial growth was developed with the help of solution deposition by Royer already in 1928,[82] resulting in a set of rules base on crystal-structure considerations that describe the fundamentals of epitaxy, up to know solution epitaxy is not a successful technique in respect to real-life device developments. This fact is surprising in view of the manifold of industrially semiconductor structures, that are manufactured by vapor phase epitaxial growth, finding applications in lighting, lasing, and in all kinds of electronics. Solution epitaxial growth is ideally suited for lead-halide-perovskites,[39,83] and has been applied previously to demonstrate photodetectors[84] and microcrystalline lasers, that have been tested up to know without passivating their surfaces [see Table S3 (Supporting Information) and references therein]. Here, surface passivation by organic ligands (TOPO), and by PMMA has been demonstrated to provide greatly positive effects on (opto-)electronic properties in general, and on laser emission, and photodetection in particular. Further improvements by surface passivation are certainly possible by fine-tuning ligand-perovskite surface interactions. For that purpose, ligand species that are currently explored in the field of perovskite solar cells or optoelectronics can be applied, such as the chloride-N,N-dimethyl selenourea complex, a multi-anchoring ligand to significantly enhance perovskite crystallinity, to suppress defect formation, and dramatically improve moisture resistance and overall stability.[85] If electrical conductivity is an issue, then for example iodotrimethylsilane[86,87] could be considered, from which the iodine ions are used for passivation, similarly as when an alkyl ammonium iodide-based ligand is used.[88] Certainly, also all ligands that have been applied in perovskite displays are possible candidates for passivation of epitaxial perovskite structures, such as those listed in ref. [89] or as the phospholipid capping ligands that have been designed for increasing the luminescence of metal halide nanocrystals.[90] All of these ligands have the potential to outperform TOPO and PMMA, however, they will not make a further as significant improvement any more as TOPO and PMMA already made in respect to the non-passivated reference. As an example, the transient luminescence in Figure 4c is already diffusion-limited, and according to the fitted model non-radiative recombination takes place solely due to charge transfer from the perovskite microstructure to the substrate. The lasing threshold, on the other hand, still has a long way to improve until something like continuous wave (cw) operation could be obtained. This can, however, possibly only be achieved by the growth of quantum structures, such as quantum dots or quantum wells in a solid matrix, since even in vapor-phase grown epitaxial bulk Gallium Arsenide, no cw laser operation can be achieved at room temperature. Thus, the surface passivation, which was demonstrated here for both, solution epitaxial as well as vapor deposition epitaxial structures, represents an important milestone for epitaxial metal-halide-perovskite micro- and nanostructures. Aside to the (opto-) electronic properties and device performance in photoconductors and lasers the epitaxial growth combined with ligand passivation tackles the most serious

disadvantage of lead-halide perovskites, that is, environmental instability. The solution epitaxial growth results in single-crystalline materials without grain boundaries, which enable fast penetration of water into the materials, and the additional surface passivation protects their surfaces from direct contact with water. Both effects retard degradation in respect to polycrystalline layers, induced for instance by a transformation of the perovskites into wide-band-gap hydrate compounds.[90] Thus, by the surface passivation introduced here for epitaxial lead-halide perovskites, two important properties, namely the optoelectronic performance as well as the stability, has been achieved. This will possibly change the epitaxial growth solution from being a non-successful technology to an option, which is worth to be considered also for commercial applications. The latter can benefit from the facile scalability and applicability of both the solution epitaxial growth and the solution-based-passivation. The last hindrance towards a commercial use of solution epitaxial growth is probably given by the fact, that the semiconductor industry prefers to process large scale epitaxial films rather than microcrystal arrangements. Continuous films could also be achieved from the lead-halide-perovskites, based on the availability of largescale substrates, which provide, next to a proper lattice parameter, also a suitable surface energy to enable a layer-by-layer epitaxial growth mode.

## 4. Conclusion

We have epitaxially grown archetypal lead-halide perovskites, including $FAPbBr_3$ via solution processing and $CsPbBr_3$ via vapor deposition, resulting in well-faceted microcubes and triangular nanowires to evaluate the effects of surface passivation. The passivating agents were chosen based on their established efficacy in colloidal nanocrystals or as protective matrices for perovskites. The attachment of these passivating species was indirectly confirmed through the advanced water resistance of the epitaxial structures, with PMMA providing more pronounced protection than TOPO. Both passivating agents act as Lewis bases, preferentially binding to cations on the perovskite surfaces.

The effectiveness of surface passivation is demonstrated through several observations: boosted photoluminescence intensity compared to un-passivated references, a record-low laser threshold power for epitaxial perovskite microcrystal lasers, and increased detectivity in nanowire networks. These results underscore the importance of surface passivation in epitaxial bromide-based perovskite structures, paralleling its significance in polycrystalline and single-crystal samples. This contrasts with lead-iodide perovskites, for which defect-free surfaces have been theoretically predicted to lack trap states.[91] However, the situation aligns more closely with colloidal nanocrystals, where dangling bonds of surface $Br^-$ ions are known to create deep trap states that can be effectively passivated by the addition of ions to the surface.[92]

By transferring insights from the field of nanocrystals—particularly surface passivation strategies involving polymers or ligands—and applying them to epitaxially grown structures, typically obtained via vapor deposition of all-inorganic compounds, we observed outstanding advancements. This approach may also apply to structures grown by molecular beam epitaxy of other semiconductors, including conventional materials, highlighting its broader relevance.

## 5. Experimental Section

*Chemicals*: Formamidinium bromide (FABr) was obtained from Greatcell Solar. Lead bromide (PbBr 98%), N, N-dimethylformamide (DMF, anhydrous, 99.8%), Toluene (anhydrous, 99.8%), cesium bromide (CsBr, 99%), TOPO (99%), PMMA (average $M_w$ ≈15 000 by GPC), and $\gamma$-butyrolactone (GBL, 99%) were sourced from Sigma-Aldrich. Bromine (99%) was procured from Acros Organics, and high-purity methanol was supplied by Alfa Aesar. All chemicals were used as received without further purification.

*Substrates*: PbS single crystals were grown using the self-selecting vapor growth method.[93] Substrate slides were cleaved from the single crystals along the {100} crystallographic planes using a blade.

*Substrates Activation*: The PbS substrates were immersed for 5 s in a 0.125% (mass concentration) bromine/methanol solution to activate the surface. Following immersion, the substrates were rinsed twice with pure methanol and dried using compressed air. The surface activation was performed immediately before material deposition.

*$FAPbBr_3$ Microcrystals Epitaxially Grown by Drop Casting*: $FAPbBr_3$ precursor solutions were prepared at a concentration of 0.1 M by combining stoichiometric amounts of FABr and $PbBr_2$ in a DMF/GBL mixture with a 1:1 volume ratio. After surface activation, the substrates were placed on a hotplate maintained at 120 °C. Subsequently, 1.5 µL droplets of the precursor solution were deposited onto the substrates using a micropipette, and the solvents were allowed to evaporate for 3 min under ambient conditions.

*$CsPbBr_3$ Nanowires Epitaxially Grown by Chemical Vapor Deposition*: $CsPbBr_3$ films were prepared via co-evaporation of CsBr and $PbBr_2$ onto freshly cleaved V1-grade 2.5 × 2.5 $cm^2$ muscovite mica substrates in a physical vapor deposition system. The substrates were maintained at 375 °C during growth. Deposition rates of CsBr and $PbBr_2$ were controlled using quartz crystal microbalances, set at 0.1 and 0.14 Å $s^{-1}$, respectively, and the process lasted for 10 000 s. A slight excess of $PbBr_2$ was supplied to offset its relatively high re-evaporation rate at the elevated substrate temperature. To ensure uniform deposition, the substrate was rotated at 2 rpm throughout the process.

*Surface Treatment of Epitaxial $FAPbBr_3$ Microcrystals*: TOPO (10 mg) and PMMA (2.5 mg) were individually dissolved in 1 mL of toluene. For the passivation process, ≈2 µL of the respective passivation solution was deposited onto the sample, followed by spin-coating at 2000 rpm for 60 s. The sample was then annealed on a hotplate at 120 °C for 5 min, subsequently cooled to room temperature, and the entire process was conducted in air.

*Surface Treatment of $CsPbBr_3$ Nanowires*: PMMA (10 mg) was dissolved in 1 mL of toluene. The passivation process was conducted by depositing ≈10 µL of the passivation solution onto the sample to ensure the solution completely covered the 1.5 × 1.5 $cm^2$ sample, followed by immediate spin coating at 2000 rpm for 60 s. The sample was then annealed on a hot plate at 120 °C for 5 min and subsequently cooled to room temperature.

*Synthesis of Caesium Lead Bromide Nanocrystals*: CsPbBr3 nanocrystals embedded in a PMMA matrix were prepared according to the procedure reported by Protesescu et al.[60] To prepare the nanocrystals, a mixture of 0.188 mmol lead bromide and 5 mL octadecene was added to a 25 mL three-neck flask. This mixture was dried under vacuum for 2 h at 120 °C using standard Schlenk line techniques. Subsequently, the atmosphere was changed to argon, and 0.5 mL pre-distilled oleic acid and 0.5 mL pre-distilled oleyl amine were injected to solubilize the lead bromide. Once the solution became clear, the temperature was raised to 160 °C. At this point, 0.4 mL of a preheated caesium oleate stock solution (0.125 M in octadecene) was promptly injected. After 5 s, the growth was quenched by placing the flask in an ice-water bath. The resulting nanocrystals were isolated from the reaction mixture by centrifugation at 6000 rpm for 30 min, and the pellet was redispersed in 3 mL toluene.

*Embedding of $CsPbBr_3$ Nanocrystals into PMMA Polymer*: For the PMMA polymerization, 60 µL of the nanocrystal stock solution was combined with 500 µL of methyl methacrylate. The residual toluene was first removed under vacuum. Subsequently, 5 mg of the photoinitiator

phenyl-bis (2,4,6-Trimethylbenzoyl) phosphinoxid (BAPO) was dissolved in the nanocrystal-monomer mixture. The final solution was then spread onto a glass substrate and polymerized using an 8 W, 365 nm UV lamp until a solid film formed.

*Electron Microscopy*: SEM was performed using a JEOL JSM-7610F Schottky field-emission scanning electron microscope, equipped with an X-MAX 80 EDS detector (Oxford Instruments).

*Photoluminescence Measurement*: Steady state PL spectra were measured using a 375 nm laser as the excitation source, and a 420 nm long-pass filter.

*Hyperspectral Photoluminescence Imaging*: The photoluminescence (PL) emission maps were acquired using a wide-field, hyperspectral imaging microscope (Photon etc. IMA VIS). A continuous-wave, power-tunable 405 nm laser was used as the PL excitation source. A 50× microscope objective was used, and the images were captured with a camera (CCD, EMCCD, sCMOS). The setup enabled the recording of spectrally resolved images with a spectral resolution of 2 nm and a spatial resolution of 0.53 µm.

*Time-Resolved Photoluminescence*: The TrPL signal was excited with a 402 nm laser with a repetition rate of 0.5 MHz and collected with a FluoTime 300 system.

*Laser Spot Size*: It was determined by using Raspberry Pi 4B and Raspberry Pi HQ camera module with a script (https://github.com/koopaduo2/Beam-GUI). It is noted that the infrared filter of the HQ camera was removed to minimize the distance between the lens of the microscope and the sensor of the camera and to ensure the focus position is properly aligned. In addition, to avoid saturating the up limit of the HQ camera, one or several neutral filters were used when using different magnification objectives.

*Solving the Rate Equation Model*: The rate equation with the diffusion term is solved for the excess charge carrier concentration using a 1D finite element model, that extends over 10 µm from the surface of the micro crystal to the substrate. The discretization in space is carried out with a sufficiently high number of linear finite elements, and a fourth-order Runge-Kutta method is used for time integration. As initial conditions, it is assumed that the excess charge carrier concentration and the density of occupied electron traps are zero everywhere. Excess charge carriers are then generated close to the surface to represent illumination by a laser pulse. The evolution of the excess charge carrier concentration due to diffusion, band-to-band recombination, and recombination via trap states is simulated within the micro crystal for 1–5 µs.

*NAP-XPS Experiments*: The XPS measurements were conducted on freshly prepared samples with sufficient dimensions well above the spatial resolution of the used EnviroESCA device (Specs) with a monochromatized Al $K_\alpha$ source (1486.71 eV). Signal detection was performed using a Phoibos 150 NAP 1D-DLD (Specs) hemispherical analyzer in Fixed Analyzer Transmission (FAT) regime. The raw data were analyzed without peak shifting to compensate for sample charging, except when explicitly states, by making use of CasaXPS software. The background was considered in these fits by a straight-line spanning over the energy region of interest.

*Lasing Measurements*: A 532 nm pulsed ns laser with a repetition rate of 1 kHz and pulse width of 1.3 ns was used to carry out optically pumped lasing measurements on single $FAPbBr_3$ micro-crystallites in ambient conditions at room temperature. The pump laser was introduced into a home-built optical microscope and focused on the sample by an 32X, NA 0.5 objective. The emission from the microcrystal was collected with the same objective and the pump laser line was blocked with a 550 nm long-pass filter. The photoluminescence spectra were recorded using AvaSpec-ULS2048L spectrometer from AVANTES with 600 $mm^{-1}$ grating and resolution FWHM of 0.7 nm. Photoluminescence images were taken using BRESSER Mikro CamII 5MP HIS microscope camera.

*Atomic Force Microscopy*: The AFM measurement was performed by a Hitachi AFM5200s scanning probe microscope in the dynamic force microscope mode.

*X-Ray Characterization*: The XRD $2\theta/\theta$ pattern was measured by a Malvern Panalytical Empyrean diffractometer operating at 45 kV and 40 mA with a Ge (220) two-bounce monochromator (Cu K$\alpha$1 $\lambda = 1.5406$).

*Photoconductivity Characterization*: Photoconductor devices were fabricated in a coplanar geometry with two carbon electrodes (Dyenamo) separated by a distance of 1 mm. After deposition of carbon paste, the samples were annealed for 15 min at 120 °C. Photogeneration was obtained using a conventional tungsten halogen lamp coupled with an Acton SP2150i monochromator. The light source was focused uniformly onto the sample and modulated with a chopper at 10 Hz. A bias of 85 V was applied using a Keithley 2612B source measure unit, and the resulting photocurrent was measured across a 1 MΩ series resistor with a Stanford Research Systems SR830 DSP lock-in amplifier. Noise measurements were performed using the same lock-in amplifier with its internal oscillator as a reference.

## Supporting Information

Supporting Information is available from the Wiley Online Library or from the author.

## Acknowledgements

Z.P. and S.Z. acknowledge the financial support from the China Scholarship Council. W.H., V.R., and Y.H. acknowledge financial support from the Deutsche Forschungsgemeinschaft (DFG), project No. GRK2495/J, and C.J.B. from GRK2495/E, and J.M. from GRK2495/C. The authors gratefully acknowledge funding from the German Federal Ministry of Education and Research (BMBF) for the Solar TAP innovation platform under the Helmholtz Innovation Platforms funding line. The work of JK and TS was partially supported by the "MagTop" project(FENG.02.01-IP.05-0028/23) carried out within the "International ResearchAgendas" programme of the Foundation for Polish Science co-financed by the European Union under the European Funds for Smart Economy 2021-2027 (FENG). The authors gratefully acknowledge the use of the services and facilities of the Energie Campus Nürnberg and the CERIC-ERIC Consortium for access to experimental facilities at LRI SPL-HTC in Prague (Proposal number: Fast Track 20257149).

Open access funding enabled and organized by Projekt DEAL.

## Conflict of Interest

The authors declare no conflict of interest.

## Data Availability Statement

The data that support the findings of this study are openly available in Zenodo at 10.5281/zenodo.17481640, reference number 17481640.

## Keywords

$CsPbBr_3$, epitaxy, $FAPbBr_3$, lasing, micro-resonators, passivation, perovskites, photoconductivity

Received: October 30, 2025
Revised: November 3, 2025
Published online: November 19, 2025

[1] J. Wang, Y. Liu, X. Wei, *J. Cryst. Growth* **2024**, *637*, 127742.
[2] G. Srinivasan, *J. Cryst. Growth* **1984**, *70*, 201.
[3] H. Iwamoto, H. Kondo, Y. Yu, A. Kawakami, M. Nakaoka, *IEE Proc.s-Electric Power Applications* **2001**, *148*, 443.
[4] H. Hamada, *Materials* **2017**, *10*, 875.

[5] D. Feezell, S. Nakamura, *C. R. Phys.* **2018**, *19*, 113.
[6] F. Capasso, *Science* **1987**, *235*, 172.
[7] M. A. Green, E. D. Dunlop, M. Yoshita, N. Kopidakis, K. Bothe, G. Siefer, X. Hao, J. Y. Jiang, *Prog. Photovoltaics* **2025**, *33*, 795.
[8] H. Chen, C. Liu, J. Xu, A. Maxwell, W. Zhou, Y. Yang, Q. Zhou, A. S. R. Bati, H. Wan, Z. Wang, L. Zeng, J. Wang, P. Serles, Y. Liu, S. Teale, Y. Liu, M. I. Saidaminov, M. Li, N. Rolston, S. Hoogland, T. Filleter, M. G. Kanatzidis, B. Chen, Z. Ning, E. H. Sargent, *Science* **2024**, *384*, 189.
[9] N. Cheng, W. Li, D. Zheng, W. X. Yang, *ChemPlusChem* **2023**, *88*, 202300367.
[10] J. Xia, C. Liang, S. Mei, H. Gu, B. He, Z. Zhang, T. Liu, K. Wang, S. Wang, S. Chen, Y. Cai, G. Xing, *J. Mater. Chem. A* **2021**, *9*, 2919.
[11] Q. Jiang, Y. Zhao, X. Zhang, X. Yang, Y. Chen, Z. Chu, Q. Ye, X. Li, Z. Yin, J. You, *Nat. Photonics* **2019**, *13*, 460.
[12] Z. Zhou, H. W. Qiao, Y. Hou, H. G. Yang, S. Yang, *Energ. Environ Sc.* **2021**, *14*, 127.
[13] Y. Lei, Y. Chen, R. Zhang, Y. Li, Q. Yan, S. Lee, Y. Yu, H. Tsai, W. Choi, K. Wang, Y. Luo, Y. Gu, X. Zheng, C. Wang, C. Wang, H. Hu, Y. Li, B. Qi, M. Lin, Z. Zhang, S. A. Dayeh, M. Pharr, D. P. Fenning, Y.-H. Lo, J. Luo, K. Yang, J. Yoo, W. Nie, S. Xu, *Nature* **2020**, *583*, 790.
[14] Y. Wu, J. Feng, Z. Yang, Y. Liu, S. F. Liu, *Adv. Sci. (Weinh)* **2022**, *10*, 2205536.
[15] Y. He, L. Matei, H. J. Jung, K. M. McCall, M. Chen, C. C. Stoumpos, Z. Liu, J. A. Peters, D. Y. Chung, B. W. Wessels, M. R. Wasielewski, V. P. Dravid, A. Burger, M. G. Kanatzidis, *Nat.Commun* **2018**, *9*, 1609.
[16] Y. Song, L. Li, W. Bi, M. Hao, Y. Kang, A. Wang, Z. Wang, H. Li, X. Li, Y. Fang, D. Yang, Q. Dong, *Research (Wash D C)* **2020**, *2020*, 5958243.
[17] J. Ko, B. Park, J. Byun, S. Pandey, A. Jo, J. H. Lee, W. Lee, J. W. Lee, N. G. Park, M. J. Lee, *InfoMat* **2024**, *6*, 12560.
[18] S. Teale, M. Degani, B. Chen, E. H. Sargent, G. Grancini, *Nat.Energy* **2024**, *9*, 779.
[19] L. Zhou, J. Su, Z. Lin, X. Guo, J. Ma, T. Li, J. Zhang, J. Chang, Y. Hao, *Research* **2021**, *2021*, 9836752.
[20] L. Chen, H. Wang, W. Zhang, F. Li, Z. Wang, X. Wang, Y. Shao, J. Shao, *ACS Appl. Mater. Interfaces.* **2022**, *14*, 10917.
[21] A. Feng, S. Xie, X. Fu, Z. Chen, W. Zhu, *Front. Chem.* **2021**, *9*, 823868.
[22] Z. Zhang, W. Kim, M. J. Ko, Y. Li, *Nano Convergence* **2023**, *10*, 23.
[23] N. He, L. Zhang, X. He, J. Guo, X. Wu, Q. Li, J. He, *Adv.Opt .Mater* **2024**, *12*, 2400707.
[24] F. Cui, P. Zhang, L. Zhang, Y. Hua, X. Sun, X. Li, G. Zhang, X. Tao, *Chem. Mater.* **2022**, *34*, 9601.
[25] L. Zhang, L. Liu, P. Zhang, R. Li, G. Zhang, X. Tao, *ACS Appl. Mater. Interfaces.* **2020**, *12*, 39834.
[26] K. Nasyedkin, I. King, L. Zhang, P. Chen, L. Wang, R. J. Staples, R. R. Lunt, J. Pollanen, *iScience* **2021**, *24*, 102912.
[27] J. Chen, Y. Fu, L. Samad, L. Dang, Y. Zhao, S. Shen, L. Guo, S. Jin, *Nano Lett.* **2017**, *17*, 460.
[28] H. K. D. Le, Y. Zhang, P. Behera, A. Vailionis, A. Phang, R. M. Brinn, P. Yang, *Nano Lett.* **2024**, *24*, 5189.
[29] Y. Wang, X. Sun, R. Shivanna, Y. Yang, Z. Chen, Y. Guo, G.-C. Wang, E. Wertz, F. Deschler, Z. Cai, H. Zhou, T.-M. Lu, J. Shi, *Nano Lett.* **2016**, *16*, 7974.
[30] J. Rieger, T. Kißlinger, A. Raabgrund, J. Hauner, D. Niesner, M. A. Schneider, T. Fauster, *Phys. Rev. Mater.* **2023**, *7*, 035403.
[31] Q. Zhang, R. Su, X. Liu, J. Xing, T. C. Sum, Q. Xiong, *Adv. Funct. Mater.* **2016**, *26*, 6238.
[32] M. Han, J. Sun, M. Peng, N. Han, Z. Chen, D. Liu, Y. Guo, S. Zhao, C. Shan, T. Xu, *J. Phys. Chem. C* **2019**, *123*, 17566.
[33] D. Kong, Y. Zhang, D. Cheng, E. Wang, K. Zhang, H. Wang, K. Liu, L. Yin, X. Sheng, *ACS Appl. Mater. Interfaces.* **2022**, *14*, 52508.
[34] Y. Wang, Y. Shi, G. Xin, J. Lian, J. Shi, *Cryst. Growth Des.* **2015**, *15*, 4741.
[35] Y. Wang, X. Sun, R. Shivanna, Y. Yang, Z. Chen, Y. Guo, G.-C. Wang, E. Wertz, F. Deschler, Z. Cai, *Nano Lett.* **2016**, *16*, 7974.
[36] G. Tang, P. You, Q. Tai, A. Yang, J. Cao, F. Zheng, Z. Zhou, J. Zhao, P. K. L. Chan, F. Yan, *Adv. Mater.* **2019**, *31*, 1807689.
[37] E. Shi, B. Yuan, S. B. Shiring, Y. Gao, Akriti, Y. Guo, C. Su, M. Lai, P. Yang, J. Kong, B. M. Savoie, Y. Yu, L. Dou, *Nature* **2020**, *580*, 614.
[38] Y. Lei, Y. Li, C. Lu, Q. Yan, Y. Wu, F. Babbe, H. Gong, S. Zhang, J. Zhou, R. Wang, R. Zhang, Y. Chen, H. Tsai, Y. Gu, H. Hu, Y.-H. Lo, W. Nie, T. Lee, J. Luo, K. Yang, K.-I. Jang, S. Xu, *Nature* **2022**, *608*, 317.
[39] M. V. Kelso, N. K. Mahenderkar, Q. Chen, J. Z. Tubbesing, J. A. Switzer, *Science* **2019**, *364*, 166.
[40] Y. Xu, X. Wang, J. Zhao, Y. Pan, Y. Li, E. E. Elemike, Q. Li, X. Zhang, J. Chen, Z. Zhao, *Front. Mater.* **2021**, *8*, 651957.
[41] H. Min, N. Wang, N. Chen, Y. Tong, Y. Wang, J. Wang, J. Liu, S. Wang, X. Wu, P. Yang, H. Shi, C. Zhuo, Q. Chen, J. Li, D. Zhang, X. Lu, C. Zhu, Q. Peng, L. Zhu, J. Chang, W. Huang, J. Wang, *Nat. Nanotechnol.* **2024**, *19*, 632.
[42] L. Huang, Q. Gao, L. D. Sun, H. Dong, S. Shi, T. Cai, Q. Liao, C. H. Yan, *Adv. Mater.* **2018**, *30*, 1800596.
[43] L. Zhao, Z. Shi, Y. Zhou, X. Wang, Y. Xian, Y. Dong, O. Reid, Z. Ni, M. C. Beard, Y. Yan, J. Huang, *Nat. Photonics* **2024**, *18*, 250.
[44] X. Qiao, R. Zhu, D. Yan, Z. Su, Z. Zhang, H. Wu, Y. Tan, M. Liang, W. Zuo, J. Zhang, G. Li, X. Gao, M. Saliba, M. Li, *Adv. Funct. Mater.* **2024**, *34*, 2409852.
[45] R. Wang, J. Xue, K.-L. Wang, Z.-K. Wang, Y. Luo, D. Fenning, G. Xu, S. Nuryyeva, T. Huang, Y. Zhao, *Science* **2019**, *366*, 1509.
[46] Y. Cao, F. Gao, L. Xiang, H. Li, D. Li, Q. Liu, H. Liu, C. Zou, S. Li, *Adv. Mater. Interfaces* **2022**, *9*, 2200179.
[47] J. Ye, M. M. Byranvand, C. O. Martinez, R. L. Z. Hoye, M. Saliba, L. Polavarapu, *Angew Chem Int Ed Engl* **2021**, *60*, 21636.
[48] C.-T. Lin, F. De Rossi, J. Kim, J. Baker, J. Ngiam, B. Xu, S. Pont, N. Aristidou, S. A. Haque, T. Watson, *J. Mater. Chem. A* **2019**, *7*, 3006.
[49] C. Murray, D. J. Norris, M. G. Bawendi, *J. Am. Chem. Soc.* **1993**, *115*, 8706.
[50] F. V. Mikulec, M. Kuno, M. Bennati, D. A. Hall, R. G. Griffin, M. G. Bawendi, *J. Am. Chem. Soc.* **2000**, *122*, 2532.
[51] F. Pinaud, D. King, H.-P. Moore, S. Weiss, *J. Am. Chem. Soc.* **2004**, *126*, 6115.
[52] D. W. DeQuilettes, S. Koch, S. Burke, R. K. Paranji, A. J. Shropshire, M. E. Ziffer, D. S. Ginger, *ACS Energy.Lett* **2016**, *1*, 438.
[53] L. Li, Y. Hu, Y. Chen, C. Wang, G. Zhao, X. Du, C. Wang, L. Xiao, Z. Lu, J. Wang, *Adv. Funct. Mater.* **2023**, *33*, 2301205.
[54] F. Yang, H. E. Lim, F. Wang, M. Ozaki, A. Shimazaki, J. Liu, N. B. Mohamed, K. Shinokita, Y. Miyauchi, A. Wakamiya, *Adv. Mater. Interfaces* **2018**, *5*, 1701256.
[55] Yukta, M. K. Chini, R. Ranjan, S. Satapathi, *ACS Appl. Electron. Mater.* **2021**, *3*, 1572.
[56] X. Wu, X.-F. Jiang, X. Hu, D.-F. Zhang, S. Li, X. Yao, W. Liu, H.-L. Yip, Z. Tang, Q.-H. Xu, *Nanoscale* **2019**, *11*, 1959.
[57] S. Zhou, V. Rehm, H. A. Afify, Y. Han, J. Korczak, A. Szczerbakow, T. Story, Z. Peng, A. These, A. Barabash, *Adv. Funct. Mater.* **2024**, *34*, 2404700.
[58] L. Zhao, Z. Shi, Y. Zhou, X. Wang, Y. Xian, Y. Dong, O. Reid, Z. Ni, M. C. Beard, Y. Yan, *Nat. Photonics* **2024**, *18*, 250.
[59] Y. Yao, H. Yu, Y. Wu, Y. Lu, Z. Liu, X. Xu, B. Ma, Q. Zhang, S. Chen, W. Huang, *ACS Omega* **2019**, *4*, 9150.
[60] L. Protesescu, S. Yakunin, M. I. Bodnarchuk, F. Krieg, R. Caputo, C. H. Hendon, R. X. Yang, A. Walsh, M. V. Kovalenko, *Nano Lett.* **2015**, *15*, 3692.
[61] H. Bhatia, B. Ghosh, E. Debroye, *J.Mater .Chem .C* **2022**, *10*, 13437.
[62] D. Vorontsov, M. Ledinský, A. Vlk, R. Hlaváč, L. Landová, T. Kosutová, K. Knížek, A. Fučíková, N. Mrkyvkova, P. Siffalovic, J. Valenta, *J. Phys. Chem. C* **2025**, *129*, 14190.
[63] A. These, N. H. Khansur, O. Almora, L. Luer, G. J. Matt, U. Eckstein, A. Barabash, A. Osvet, K. G. Webber, C. J. Brabec, *Adv.Electron.Mater* **2021**, *7*, 2001165.

[64] M. S. Hammer, H. Schlott, L. Lüer, C. J. Brabec, M. Sytnyk, J. Will, B. Meyer, W. Heiss, *Nat. Rev. Mater.* **2025**, *10*, 311.
[65] R. Ferreira, M. Shaikh, S. K. Jakka, J. Deuermeier, P. Barquinha, S. Ghosh, E. Fortunato, R. Martins, S. Jana, *Nano Lett.* **2022**, *22*, 9020.
[66] M. Yao, J. Jiang, D. Xin, Y. Ma, W. Wei, X. Zheng, L. Shen, *Nano Lett.* **2021**, *21*, 3947.
[67] Y. Sun, X. Yang, W. Jiao, J. Wu, Z. Zhao, *ACS Appl. Electron. Mater.* **2021**, *3*, 415.
[68] C. Li, X. Wang, E. Bi, F. Jiang, S. M. Park, Y. Li, L. Chen, Z. Wang, L. Zeng, H. Chen, Y. Liu, C. R. Grice, A. Abudulimu, J. Chung, Y. Xian, T. Zhu, H. Lai, B. Chen, R. J. Ellingson, F. Fu, D. S. Ginger, Z. Song, E. H. Sargent, Y. Yan, *Science* **2023**, *379*, 690.
[69] Q. Sun, B. Tuo, Z. Ren, T. Xue, Y. Zhang, J. Ma, P. Li, Y. Song, *Adv. Funct. Mater.* **2022**, *32*, 2208885.
[70] H. Wang, Y. Wei, H. Li, X. Zhang, H. Qi, B. Tang, Y. Guo, L. Ye, H. Wang, *Adv. Mater. Interfaces* **2021**, *8*, 2100442.
[71] A. Sadhu, Y. Guo, T. Salim, Q. Sun, S. G. Mhaisalkar, T. C. Sum, L. H. Wong, *Adv. Funct. Mater.* **2023**, *33*, 2305215.
[72] H. Chen, L. Fan, R. Zhang, C. Bao, H. Zhao, W. Xiang, W. Liu, G. Niu, R. Guo, L. Zhang, *Adv.Opt .Mater* **2020**, *8*, 1901390.
[73] C. Liu, Y. Yang, H. Chen, J. Xu, A. Liu, A. S. Bati, H. Zhu, L. Grater, S. S. Hadke, C. Huang, *Science* **2023**, *382*, 810.
[74] V. V. Burungale, R. S. Devan, S. A. Pawar, N. S. Harale, V. L. Patil, V. Rao, Y.-R. Ma, J. E. Ae, J. H. Kim, P. S. Patil, *Mater. Sci.-Poland* **2016**, *34*, 204.
[75] Y. Wu, L. Liu, W. Wang, W. Zhang, H. Yu, J. Qian, Y. Chen, W. Shen, S. Sui, Z. Deng, S. Chen, W. Huang, *J.Mater .Chem .C* **2020**, *8*, 9936.
[76] V. Milotti, S. Cacovich, D. R. Ceratti, D. Ory, J. Barichello, F. Matteocci, A. Di Carlo, P. M. Sheverdyaeva, P. Schulz, P. Moras, *Small Methods* **2023**, *7*, 2300222.
[77] Y. Wang, S. Wang, R. Li, W. Li, T. Long, L. Wang, L. Kong, F. Cao, Q. Wu, G. Jia, *Small* **2024**, *20*, 2402825.
[78] Y. Wu, L. Liu, W. Wang, W. Zhang, H. Yu, J. Qian, Y. Chen, W. Shen, S. Sui, Z. Deng, *J.Mater .Chem .C* **2020**, *8*, 9936.
[79] Z. Ahmad, A. Mishra, *J. Mater. Sci.: Mater. Electron.* **2020**, *31*, 4672.
[80] H. A. Afify, M. Sytnyk, V. Rehm, A. Barabash, O. Mashkov, A. Osvet, V. V. Volobuev, J. Korczak, A. Szczerbakow, T. Story, K. Götz, T. Unruh, C. Schüßlbauer, D. Thiel, T. Ullrich, M. D. Guldi, J. C. Brabec, W. Heiss, *Adv.Opt .Mater* **2022**, *10*.
[81] Y. Rakita, N. Kedem, S. Gupta, A. Sadhanala, V. Kalchenko, M. L. Böhm, M. Kulbak, R. H. Friend, D. Cahen, G. Hodes, *Cryst. Growth Des.* **2016**, *16*, 5717.
[82] L. Royer, *Bulletin de Minéralogie* **1928**, *51*, 7.
[83] M. Sytnyk, A. A. Yousefi-Amin, T. Freund, A. Prihoda, K. Götz, T. Unruh, C. Harreiss, J. Will, E. Spiecker, J. Levchuk, *Adv. Funct. Mater.* **2020**, *30*, 2004612.
[84] L. Ji, H.-Y. Hsu, J. C. Lee, A. J. Bard, E. T. Yu, *Nano Lett.* **2018**, *18*, 994.
[85] R. Nie, P. Zhang, J. Gao, C. Wang, W. Chu, L. Li, K. Wang, D. Qian, F. Lin, X. Xia, Y. Wu, L. Chao, C. Miao, X. Zhao, W. Guo, Z. Zhang, *Nat.Commun* **2025**, *16*, 6438.
[86] A. Vartanian, *Nat. Rev. Mater.* **2023**, *8*, 707.
[87] F. Zhao, H. W. Duan, S. N. Li, J. L. Pan, W. S. Shen, S. M. Li, Q. Zhang, Y. K. Wang, L. S. Liao, *Angew. Chem. Int. Ed. Engl.* **2023**, *62*, 202311089.
[88] H. Aqoma, S.-H. Lee, I. F. Imran, J.-H. Hwang, S.-H. Lee, S.-Y. Jang, *Nat.Energy* **2024**, *9*, 324.
[89] X. Zhang, J. Cai, L. Yang, J. Luo, T. Guo, E. L. Chen, *ACS Energy.Lett* **2024**, *9*, 1587.
[90] V. Morad, A. Stelmakh, M. Svyrydenko, L. G. Feld, S. C. Boehme, M. Aebli, J. Affolter, C. J. Kaul, N. J. Schrenker, S. Bals, Y. Sahin, D. N. Dirin, I. Cherniukh, G. Raino, A. Baumketner, M. V. Kovalenko, *Nature* **2024**, *626*, 542.
[91] O. Rubel, X. Rocquefelte, *J. Phys. Chem. C* **2024**, *128*, 5667.
[92] I. du Fossé, J. T. Mulder, G. Almeida, A. G. Spruit, I. Infante, F. C. Grozema, A. J. Houtepen, *J. Am. Chem. Soc.* **2022**, *144*, 11059.
[93] A. Szczerbakow, K. Durose, *Prog. Cryst. Growth Charact. Mater.* **2005**, *51*, 81.